The Astrophysical Journal, 964:196 (14pp), 2024 April 1 https://doi.org/10.3847/1538-4357/ad19c9

SN 2022joj: A Potential Double Detonation with a Thin Helium Shell

E. Padilla Gonzalez[1,2], D. A. Howell[1,2], G. Terreran[2], C. McCully[1,2], M. Newsome[1,2], J. Burke[1,2], J. Farah[1,2], C. Pellegrino[1,2], K. A. Bostroem[3,16], G. Hosseinzadeh[3], J. Pearson[3], D. J. Sand[3], M. Shrestha[3], N. Smith[3], Y. Dong (董一泽)[4], N. Meza Retamal[4], S. Valenti[4], S. Boos[5], K. J. Shen[6], D. Townsley[5], L. Galbany[7,8], L. Piscarreta[7], R. J. Foley[9], M. J. Bustamante-Rosell[9], D. A. Coulter[9], R. Chornock[10], K. W. Davis[9], C. B. Dickinson[9], D. O. Jones[11], J. Kutcka[9], X. K. Le Saux[9], C. R. Rojas-Bravo[9], K. Taggart[9], S. Tinyanont[12], G. Yang[13], S. W. Jha[14], and R. Margutti[10,15]

[1] Department of Physics, University of California, Santa Barbara, CA 93106-9530, USA; epadillagonzalez@ucsb.edu
[2] Las Cumbres Observatory, 6740 Cortona Drive, Suite 102, Goleta, CA 93117-5575, USA
[3] Steward Observatory, University of Arizona, 933 North Cherry Avenue, Tucson, AZ 85721-0065, USA
[4] Department of Physics and Astronomy, University of California, 1 Shields Avenue, Davis, CA 95616-5270, USA
[5] Department of Physics and Astronomy, University of Alabama, Tuscaloosa, AL 35487, USA
[6] Department of Astronomy and Theoretical Astrophysics Center, University of California, Berkeley, CA 94720, USA
[7] Institute of Space Sciences (ICE-CSIC), Campus UAB, Carrer de Can Magrans, s/n, E-08193 Barcelona, Spain
[8] Institut dEstudis Espacials de Catalunya (IEEC), E-08034 Barcelona, Spain
[9] Department of Astronomy and Astrophysics, University of California, Santa Cruz, CA 95064, USA
[10] Department of Astronomy, University of California, Berkeley, CA 94720-3411, USA
[11] Gemini Observatory/NSFs NOIRLab, 670 N. Aohoku Place, Hilo, HI 96720, USA
[12] National Astronomical Research Institute of Thailand, 260 Moo 4, Donkaew, Maerim, Chiang Mai, 50180, Thailand
[13] The Thacher School, 5025 Thacher Road, Ojai, CA 93023, USA
[14] Department of Physics and Astronomy, Rutgers, The State University of New Jersey, Piscataway NJ, USA
[15] Department of Physics, University of California, 366 Physics North MC 7300, Berkeley, CA 94720, USA
Received 2023 August 11; revised 2023 December 14; accepted 2023 December 18; published 2024 March 29

Abstract

We present photometric and spectroscopic data for SN 2022joj, a nearby peculiar Type Ia supernova (SN Ia) with a fast decline rate ($\Delta m_{15,B} = 1.4$ mag). SN 2022joj shows exceedingly red colors, with a value of approximately $B - V \approx 1.1$ mag during its initial stages, beginning from 11 days before maximum brightness. As it evolves, the flux shifts toward the blue end of the spectrum, approaching $B - V \approx 0$ mag around maximum light. Furthermore, at maximum light and beyond, the photometry is consistent with that of typical SNe Ia. This unusual behavior extends to its spectral characteristics, which initially displayed a red spectrum and later evolved to exhibit greater consistency with typical SNe Ia. Spectroscopically, we find strong agreement between SN 2022joj and double detonation models with white dwarf masses of around 1 $M_\odot$ and a thin He shell between 0.01 and 0.05 $M_\odot$. Moreover, the early red colors are explained by line-blanketing absorption from iron peak elements created by the double detonation scenario in similar mass ranges. The nebular spectra in SN 2022joj deviate from expectations for double detonation, as we observe strong [Fe III] emission instead of [Ca II] lines as anticipated, though this is not as robust a prediction as early red colors and spectra. The fact that as He shells get thinner these SNe start to look more like normal SNe Ia raises the possibility that this is the triggering mechanism for the majority of SNe Ia, though evidence would be missed if the SNe are not observed early enough.

Unified Astronomy Thesaurus concepts: Supernovae (1668); Type Ia supernovae (1728)

1. Introduction

Type Ia supernovae (SNe Ia) play a pivotal role in measuring cosmological distances and were instrumental in revealing the acceleration of the universe (Riess et al. 1998; Perlmutter et al. 1999). Furthermore, they are responsible for synthesizing the majority of the iron group elements (titanium through zinc) found throughout the universe (Iwamoto et al. 1999). Although extensively researched, their progenitor systems continue to be elusive: the nature of the companion star (degenerate, Iben & Tutukov 1984; Webbink 1984; or not, Whelan & Iben 1973) and the explosion mechanism (surface detonation, Bildsten et al. 2007; or core ignited deflagration transitioning to a detonation, Khokhlov 1991; Woosley & Weaver 1994) are all subject to debate.

Studies have explored various explosion mechanisms for white dwarfs (WDs), including a helium detonation on the surface of a sub-Chandrasekhar-mass WD. In this scenario, a sub-Chandrasekhar-mass WD accumulates He from a helium star (or He WD or C/O WD, which have helium surface layers). This accumulation has the potential to trigger an ignition at the base of the He shell. This has been suggested to be the cause of some faint and fast evolving transients such as Ca-rich transients (Perets et al. 2010). The surface explosion may also drive a shock into the core causing a subsequent detonation (also known as double detonation; Bildsten et al. 2007; Fink et al. 2010; Sim et al. 2012; Shen & Bildsten 2014). Observables can vary significantly depending on the thickness of the He shell.

One predicted signature from a surface detonation of a thick helium shell ($\gtrsim$0.05 $M_\odot$) is the production of a significant amount of ^{56}Ni, resulting in extreme UV line blanketing

[16] LSSTC Catalyst Fellow.

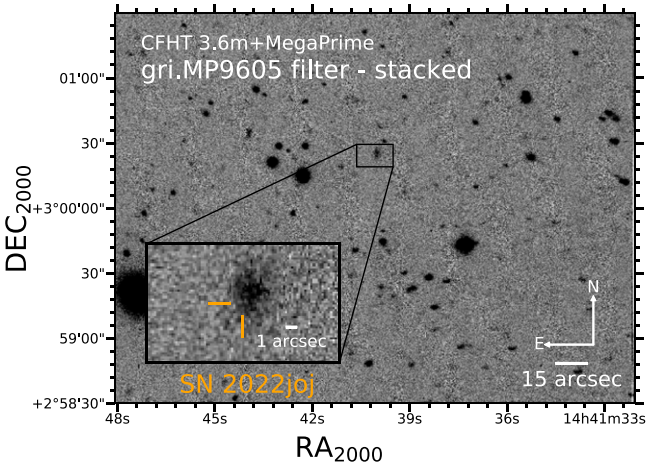

Figure 1. The host of SN 2022joj and its surroundings. The image was created by stacking six poses from CFHT+MegaPrime, obtained on two different epochs, on 2017 May 19 and 2021 April 17, both prior to SN 2022joj's explosion. The broad *gri* single filter was used for all the images.

(Kromer et al. 2010; Sim et al. 2012; Polin et al. 2019). However, it was also shown by Sim et al. (2010), Shen et al. (2018a, 2021b), Polin et al. (2019), and Boos et al. (2021) that double detonation models approaching the limiting case of a bare CO WD detonation are capable of roughly reproducing observations of SNe Ia. This is attributed to thin shell detonations mostly producing intermediate mass elements, instead of ^{56}Ni, and thus have less of an effect on the observables from the underlying core ashes.

In this paper, we discuss the peculiar SNe Ia 2022joj. This object is unique due to the strong reddening in the early spectra and light curves pointing toward a double detonation candidate. This paper is arranged as follows. In Section 2, we discuss the discovery and observations. In Section 3, we discuss reddening, light-curve, and spectral analysis. In Section 4, we compare the light curves and spectra with double detonation models and variations of ^{56}Ni distributions. Finally, in Section 5, we discuss the possible progenitor system and conclude in Section 6.

2. Discovery and Observations

2.1. Discovery

SN 2022joj was discovered by the Zwicky Transient Facility (ZTF; Sánchez-Sáez et al. 2021) on 2022 May 8, using the ZTF survey at the Palomar Observatory with a discovery magnitude of 19.1 in the *r* filter (Fremling 2022). The last nondetection of the same object was on 2022 May at 02:34 UT, with a *g* magnitude of 20.25 (Fremling 2022). An explosion time of 2459705.64 JD (or 2022 May 6,) was estimated from a power-law fits with an index of 2 to the light curve in the *r* band from time ranging between 2022 May 8 and 14. SN 2022joj is located at right ascension $14^{h}41^{m}40\overset{s}{.}07$ and declination $+03°00'24\overset{''}{.}2$ shown in Figure 1 and discussed in more detail in Section 5.2.

The Milky Way extinction value $E(B-V) = 0.0313 \pm 0.0002$ mag was adopted from the Schlafly & Finkbeiner (2011) calibration of the Schlegel et al. (1998) dust maps. Newsome et al. (2022) reported a classification on behalf of the Global Supernova Project based on a spectrum acquired on 2022 May 11, using FLOYDS on Las Cumbres Observatory's (LCO; Brown et al. 2013) Faulkes Telescope North. SN 2022joj was classified as a Type I supernova (SN) due to its lack of hydrogen, despite its uncertainty due to its spectral peculiarity. These distinctive features include suppression in the blue between 3000 and 5000 Å and the faint presence of O I.

2.2. Photometry

Following the discovery of SN 2022joj, the Global Supernova Project triggered follow-up observations and acquired photometry in the *BVgri* filters using the 1 m telescopes from the LCO global network of telescopes. The data were reduced using `lcogtsnpipe` (Valenti et al. 2016). The method utilized during the reduction was point-spread function (PSF)-fitting photometry. The *BV* zero-points were calculated from the AAVSO Photometric All-Sky Survey (APASS) standard catalog (Henden et al. 2009), whereas the *gri* zero-points were calculated from the Sloan magnitudes of field stars (Albareti et al. 2017). Additional optical photometry was retrieved from the publicly available ZTF survey.[17] In addition, imaging of SN 2022joj was obtained in *BVri* bands with the 1 m Nickel telescope at Lick Observatory. The images were calibrated using bias and sky flat-field frames following standard procedures. PSF photometry was performed, and photometry was calibrated relative to Pan-STARRS photometric standards (Flewelling et al. 2020). The full light curve is presented in Figure 2. The *BV* filters are calibrated to Vega (Bessel 1990), whereas the *gri* are calibrated in the AB magnitude system (Fukugita et al. 1996).

SN 2022joj was observed with the Ultraviolet Optical Telescope (UVOT; Roming et al. 2005) on board the Neil Gehrels Swift Observatory (Gehrels et al. 2004) for four epochs, from 2022 May 17.4 until 2022 May 22.7 ($\delta t = -5.4$ to 1.0 days from the *B*-band maximum) in the filters U, UV-W1, UV-W2, and UV-M2. We performed aperture photometry using a 5″ radius circular region with `uvotsource` within HEAsoft v6.26,[18] following the standard guidelines from Brown et al. 2009. By visual inspection, we did not discern any background contamination coming from the host galaxy; therefore, we deemed it unnecessary to perform any template subtraction. We did not detect SN 2022joj in the UV-W1 and UV-M2 filters during the first epoch, suggesting strong obscuration of the bluer part of the spectral energy distribution at early phases, as shown by the classification spectrum. The full photometric data is available in Appendix Tables A1 in the optical and A2 in the ultraviolet optical bands.

2.3. Spectra

The full spectroscopic data set is shown in Figure 3. After discovery, a follow-up sequence was initiated from the Global Supernova Project using the FLOYDS spectrographs mounted on the 2 m Faulkes Telescope North in Haleakal, Hawai'i, as well as the Faulkes Telescope South in Siding Spring, Australia. The data were reduced as detailed in Valenti et al. (2014). The redshift was initially calculated by comparing the characteristics of the observed Type Ia SN using the Supernova Identification (SNID) fitting algorithm at maximum light (Blondin & Tonry 2007). The best match at maximum light was found with SN 2000cx, resulting in a redshift of 0.024 ± 0.009. The redshift error is related to the width of the correlation peak and the `rlap` parameter, which is used to quantify the reliability of a given correlation between the input and a template spectrum (Blondin & Tonry 2007). To get a sense of the dispersion of matches obtained

[17] https://alerce.online/object/ZTF22aajijjf

[18] We used the calibration database (CALDB) version 20201008.

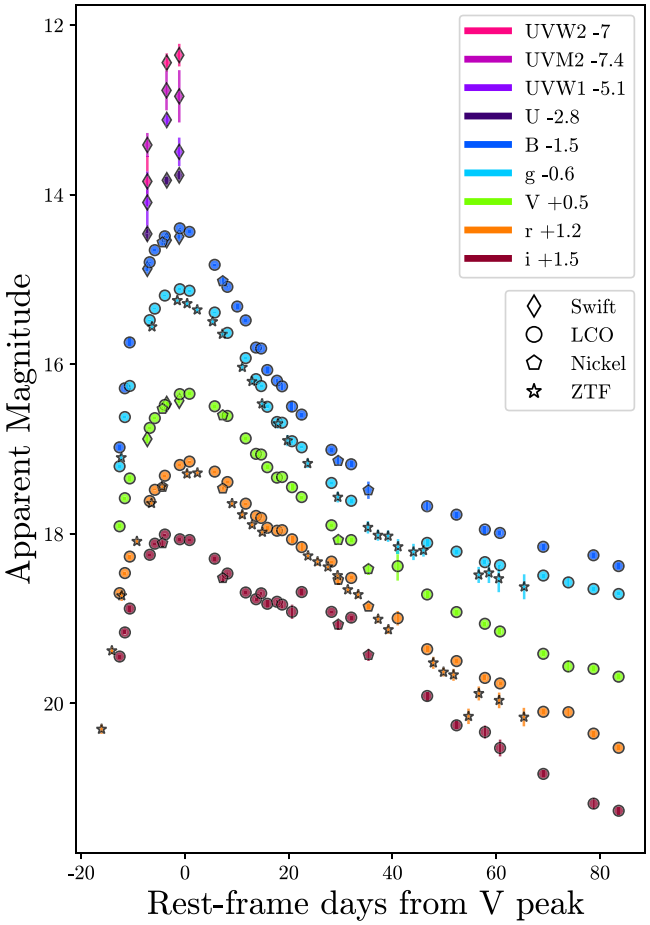

Figure 2. Milky Way extinction corrected photometry using $E(B-V)_{\rm MW} = 0.0313$ mag as discussed in Section 2. These data are not corrected for host extinction (see Section 2.2 for details on host extinction).

Table 1
Time of Maximum Light, Absolute Magnitude, and Decline Rate (Δm_{15}, the Drop in Magnitudes between Peak and 15 days after Peak) for SN 2022joj in Each Filter of Its Light Curve

Filter	$t_{\rm max}$ (JD)	$M_{\rm max}$	$\pm M_{\rm max}$	Δm_{15}
B	2459722.3	-19.54 ± 0.47	15.84 ± 0.47	1.4
g	2459722.47	-19.69 ± 0.32	15.68 ± 0.32	1.3
V	2459723.8	-19.54 ± 0.12	15.84 ± 0.12	0.85
r	2459725.63	-19.47 ± 0.12	15.9 ± 0.12	0.75
i	2459721.94	-18.91 ± 0.29	16.46 ± 0.29	0.77

Note. Note that the absolute magnitudes are corrected for Milky Way extinction.

from SNID, we examined the results of 76 potential candidates. Among them, 46 were identified as *good* matches, and those were selected to conduct a statistical analysis. We found the mean redshift to be 0.0225 with a standard deviation of 0.0057. However, Liu et al. (2023) detected H_α emission associated with the host galaxy corresponding to $z = 0.02736 \pm 0.0007$. We adopt this as the SN redshift.

All spectra were corrected for Milky Way reddening, $E(B-V) = 0.0313$ mag, as discussed in Section 2.1. We assume the host extinction to be negligible, given the uncertain local host extinction and apparent lack of visibility, coupled with no evidence of the Na ID absorption feature.

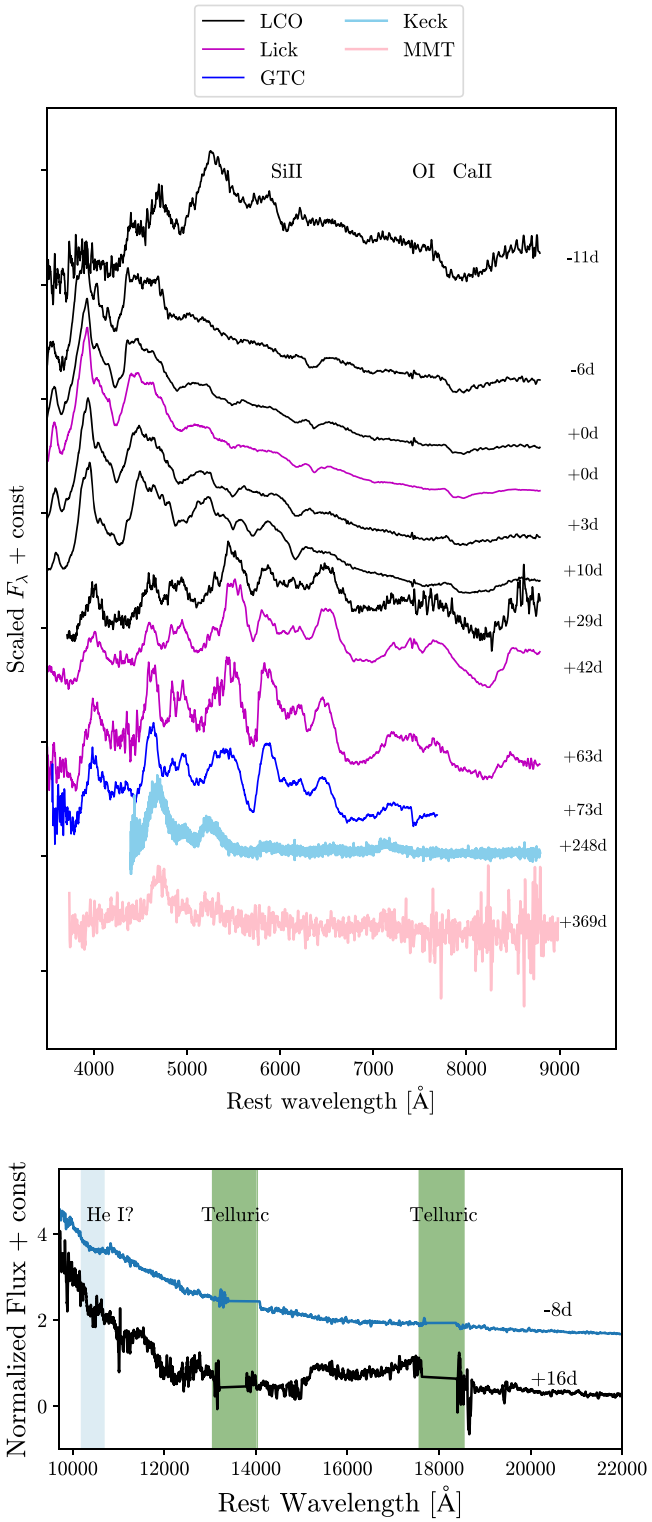

Figure 3. Milky Way extinction corrected spectra using $E(B-V)_{\rm MW} = 0.0313$ mag at various phases with respect to maximum light in the *B* band. Note, that these spectra are not corrected for host extinction (see Section 3.1 for the details on host extinction).

Multiple optical spectra were obtained from the Kast spectrograph at Lick Observatory, on 2022 May 22, June 29, and July 24. One additional spectrum was obtained from the Gran Telescopio Canarias (GTC), at the Observatorio del Roque de Los Muchachos in La Palma on 2022 August 3,

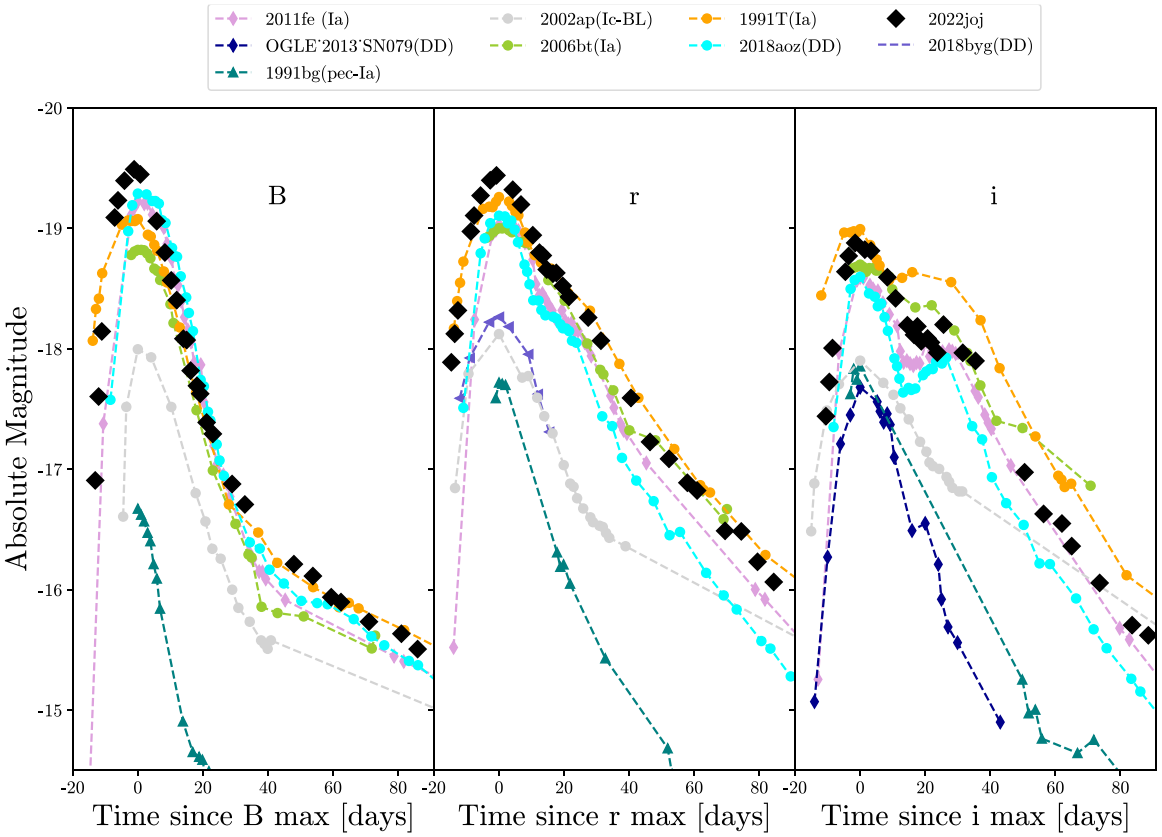

Figure 4. Extinction corrected light-curve comparison of SN 2022joj to other SNe Ia. Note that SN 2022joj declines faster than the typical SN Ia 2011fe. All of the light curves have been corrected for extinction. Note that SNe with "DD" next to their name in the legend correspond to double detonation candidates.

taken with the Optical System for Imaging and low-Intermediate-Resolution Integrated Spectroscopy (OSIRIS). The reduction process was performed using version 1.11.0 of `PypeIt` (Prochaska et al. 2020).[19] We secured a nebular spectrum from Keck+DEIMOS on 2023 January 17. `PypeIt` was used for the reduction of this latter. A second nebular spectrum was obtained with MMT+Binospec (Fabricant et al. 2019) on 2023 May 26. This was reduced automatically by the Binospec IDL pipeline (Kansky et al. 2019). Near-infrared (NIR) data from Keck taken on 2022 May 14, using the Near-Infrared Echellette Spectrometer (NIRES; Wilson et al. 2004) on the Keck II telescope. The spectrum was reduced using the Spextool software package (Cushing et al. 2004). We also acquired data from Keck Infrared Transient Survey (KITS) Collaboration on 2022 June 7 also from NIRES. These findings are visually represented in Figure 3, where the bottom plot showcases the NIRES data, and the top figure displays the optical and nebular data in ascending order.

3. Analysis

3.1. Light Curves and Colors

In order to better understand SN 2022joj's evolution over time, we present a comprehensive comparative light-curve analysis (Figure 4). The comparison encompasses the standard Type Ia, subluminous Type Ia examples like SN 1991bg (Filippenko & Richmond 1992) and SN 2002es (Ganeshalingam et al. 2012), as well as potential double detonation candidates including SN 2016hnk (Galbany et al. 2019), OGLE-2013-SN-079 (Inserra et al. 2015), SN 2016dsg (Dong et al. 2022), SN 2018aoz (Ni et al. 2022), SN 2018byg (De et al. 2019), and SN 2019eix (Padilla Gonzalez et al. 2023). Additionally, it showcases an atypical broad-line Type Ia, SN 2002bo (O'Brien et al. 2021) and draws a comparison to an energetic broad-line Type Ic, SN 2002ap (Mazzali et al. 2002). Note that all SNe are Milky Way and host extinction corrected.

Figure 4 illustrates that SN 2022joj exhibits a brighter peak absolute magnitude compared to both the standard SN Type Ia and the double detonation with a thin He shell candidate, SN 2018aoz. Additionally, from Figure 5, it is evident that the light curve's width is atypical of SNe Ia behavior. SN 2022joj does not follow the Phillips relation that links the brightness and decline rate of Type Ia SNe (Phillips 1993). Moreover, we observe that the decline rate is swifter than that of SN 2018aoz, indicating a possible less massive progenitor. These diverse observations could also be angle dependent, as discussed in Section 4.

Despite being overluminous, the light curves of SN 2022joj, as shown in Figure 4, reveal a subtle secondary maximum in the *i* band, a characteristic often observed in subluminous SNe. This behavior is attributed to their cooler SN photospheres (Kasen 2006; Foley et al. 2010), which offer valuable information about the temperature of SNe. In Figure 6, we compare the color evolution of SN 2022joj with that of typical and atypical SNe Ia, as well as double detonation candidates and models.

[19] https://github.com/pypeit/PypeIt

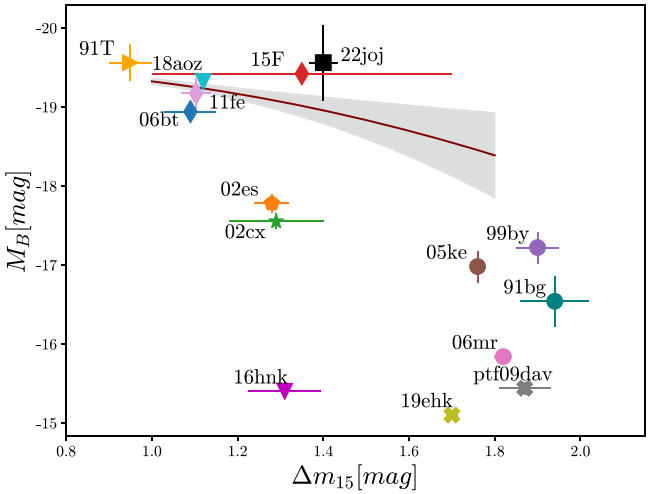

Figure 5. Phillips relation is shown in the brown line along with various peculiar SNe. Note how SN 2022joj (in black) disagrees in relation to its light-curve width. The symbols used to represent these different types are normal SNe Ia (diamonds), 91bg-like SNe Ia (circles), SNe Iax (stars), 02es-like SNe Ia (pentagons), Ca-rich objects (crosses), SN 2016hnk (down triangle), and overluminous SNe Ia 1991T (right triangle).

3.2. Spectral Analysis

Due to the remarkable features in the initial spectra of SN 2022joj, we compared it to several distinctive objects. The most prominent of these features was the suppression of the blue wavelengths ($\lambda < 5000$ Å), setting it apart from other objects as shown in Figure 7. As SN 2022joj evolved, it began to resemble a standard Type Ia. However some features commonly observed in a typical SN Ia, such as the Si II 6355 feature, were not prominent in SN 2022joj. Additionally, we also observe an absorption minimum of the Ca II triplet at a much higher velocity than the other objects throughout its evolution as shown in Figure 7.

SN 2022joj exhibits characteristics similar to those of subluminous SNe Ia approximately 5 days before reaching maximum brightness (minus the deep Si II 6355 feature and the lack of O I 7777), as evidenced by the presence of Ti II in the $4000 < \lambda < 4500$ Å range. This could be evidence of a double detonation of a He shell, since Ti is predicted to be synthesized in the high-velocity outer layers of the ejecta (Fink et al. 2010; Jiang et al. 2017) along with the high velocities of Ca II triplet, resulting from the detonation of the He shell (Fink et al. 2010; Kromer et al. 2010; Moore et al. 2013). Additionally, SN 2022joj appears to have a weak Si II 6355 and unlike the double detonation models, it appears to have a strong C II 6580 as shown in Figure 8. Similarly, in the early epochs, SN 2005bl established a presence of C II, suggesting an overall low burning efficiency with a significant amount of leftover unburned material (Taubenberger et al. 2008). However, Blondin et al. (2018) attributed this feature to absorption by the Mg II 6347 doublet in their sub-Chandrasekhar model.

At around maximum brightness, SN 2022joj continues to resemble subluminous SNe Ia spectroscopically. We also notice that the Si II 6355 feature dominates over the C II 6580 feature previously seen. Moreover, SN 2022joj shares a striking resemblance with peculiar SN 2006bt, as both share similarities with those of low-luminosity SNe Ia. Roughly 2 weeks to a month after maximum light, the Si II 6355 feature remains significantly weaker in SN 2022joj than in SN 2011fe. At the 1 month mark after maximum light, SN 2022joj bears a strong resemblance to the subluminous SN 2005bl, which displays a broad absorption trough between wavelengths of 4000 and 4500 Å, resulting from a blend of Fe group elements dominated by Ti II (Filippenko & Richmond 1992; Mazzali et al. 1997).

4. Modeling

We compared SN 2022joj with double detonation models from the existing literature due to its initial spectral peculiarities and color characteristics. We conducted photometric and spectroscopic analyses, comparing SN 2022joj with a variety of models, including those proposed by Kromer et al. (2010), Polin et al. (2019), Shen et al. (2021b), and Ni et al. (2022). In particular, Kromer et al. (2010) investigated the observable properties of double detonation models, which were simulated using the 2D radiative transport code ARTIS (Kromer & Sim 2009). These models were initialized with estimated values of temperature, central density of the CO core, and temperature and density at the base of the He layer. An initial He detonation was ignited at a single point at the base of the He shell, eventually creating a shock wave that propagated and converged into the core. The He shell masses in these models, which had previously been considered by Fink et al. (2010), ranged from 0.0035–0.0126 $M_\odot$ and WD masses spanning 0.8–1.38 $M_\odot$.

Polin et al. (2019) investigated the explosions of WDs with He shell masses of 0.01, 0.05, and 0.08 $M_\odot$ and WD masses ranging from 0.6–1.2 $M_\odot$. Thicker shell models were found to exhibit early time flux excess, redder colors, and higher line blanketing in the UV through the blue regime of the spectrum. To create these 1D models, the authors employed the Eulerian hydrodynamics code Castro (Almgren et al. 2010). Once the SN ejecta reached homologous expansion, synthetic spectra, and light curves were generated using the multidimensional time-dependent radiation transport code SEDONA (Kasen et al. 2006).

The models presented in Boos et al. (2021) and Shen et al. (2021b) utilized two-dimensional sub-Chandrasekhar-mass double detonation models as initial parameters, which were then input into the reactive hydrodynamics code FLASH (Dubey et al. 2014). To initiate the explosion in each model, a hotspot was placed along the helium shell symmetry axis. This resulted in the helium detonating around the surface to the south pole, generating a shock wave that propagated into the core and ultimately triggered a carbon-core detonation. The explosion parameters in these models varied, with core masses ranging from 0.82–1.09 $M_\odot$ and shell masses between 0.011 and 0.1 $M_\odot$. The shell masses were not comprised solely of ^{4}He, but rather were mixed with ^{12}C, ^{4}N, and ^{16}O.

Similar to Polin et al. (2019), Ni et al. (2022) He-shell double detonation 1D models, hydrodynamics, and nucleosynthesis simulations were conducted using Castro and the radiative transfer calculations were conducted using SEDONA. The parameter space covered for core masses ranged from 1.0–1.1 $M_\odot$ and the shell masses ranged from 0.01–0.012 $M_\odot$.

4.1. Light-curve Model Analysis

In Figure 9, we plot SN 2022joj light curves in the *i*, *r*, and *g* bands against various double detonation models with thin and thick He shells. We note that the SN 2022joj light-curve width and magnitude align with several of them, including Shen $0.9 + 0.1$, Polin $1.0 + 0.05$, and Ni $1.0 + 0.01$. Moreover,

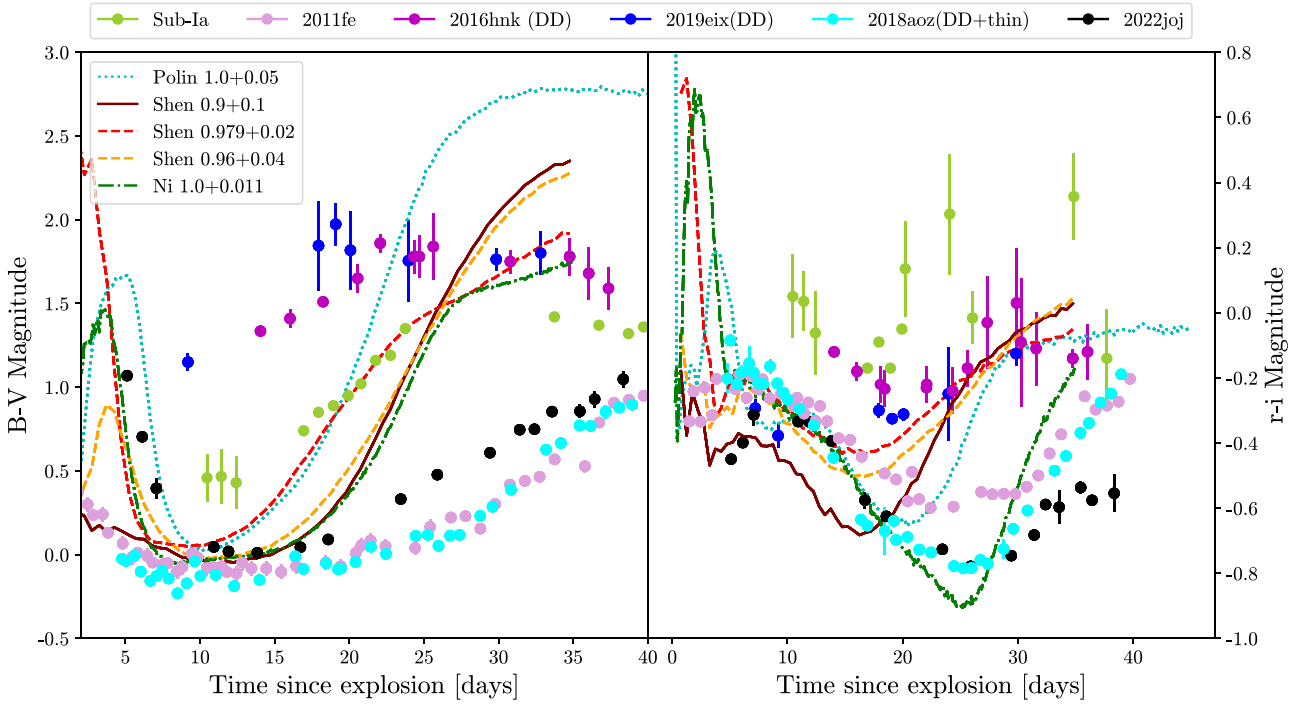

Figure 6. The color evolution of SN 2022joj plotted against other SNe in terms of explosion time, where our explosion time was calculated using a polynomial fit. We plotted double detonation models (dashed lines), where green corresponds to $1.0 + 0.011\ M_{\odot}$ from Ni et al. (2022), purple corresponds to $1.2 + 0.01\ M_{\odot}$ from Polin et al. (2019), and maroon and red correspond to Shen et al. (2021b) $0.9 + 0.1$ and $0.979 + 0.02\ M_{\odot}$. Additionally, the "Sub-Ia"category, denoting subluminous Type Ia SNe, is illustrated with data points representing SN 1991bg and SN 2005bl. Note how SN 2022joj is much redder at early phases in comparison to all of the SNe, especially SN 2011fe.

models assume local thermal equilibrium (LTE) after maximum leading to additional discrepancies, specifically a too-fast decline in *B*-band magnitude compared to more realistic non-LTE models (Shen et al. 2021b). Additionally, it is interesting to see WD masses in that mass range, since C/O WDs at formation are thought to be limited to a maximum mass of 1–1.1 $M_{\odot}$ (Dominguez et al. 1999; Girardi et al. 2002; Catalán et al. 2008). The nature of such a massive progenitor is an open question.

One possibility is that it grew by stable surface burning (H or He to C and/or O; Wolf et al. 2013), though how the progenitor could go from stable burning to helium shell detonation is unclear. A common channel found in binary population synthesis involves stable helium mass transfer from a helium star on a thermal timescale, growing the C/O WD by a couple of tenths of a solar mass. The helium star then evolves into another C/O WD, and their merger can lead to a double detonation event (Ruiter et al. 2013). Another channel could be a hypothesized hybrid C-O-Ne WD (Chen et al. 2014), sometimes invoked as the progenitors of SNe Iax (Meng & Podsiadlowski 2014). However, the Polin et al. (2019) and Shen et al. (2021b) models did not use C-O-Ne progenitors.

SN 2022joj stands out due to its extreme redness in the early stages. However, as it evolves, it appears to become more similar to a typical Ia such as SN 2011fe in terms of its colors. We explored the possibility of a double detonation involving a thin He shell as shown by Shen et al. (2018a, 2021b), Townsley et al. (2019), Boos et al. (2021), Ni et al. (2022), and Collins et al. (2022) that such events can reproduce typical SN Ia features. In Figure 6, we plot the color evolution of SN 2022joj along with double detonation models. Our analysis indicates that SN 2022joj is much redder at early epochs than SN 2011fe. Notably, the Ni $1.0 + 0.01$ (referring to a 1.0 $M_{\odot}$ WD mass with a helium shell of 0.01 $M_{\odot}$) and Shen $0.0979 + 0.02$ models, accurately predict the colors of SN 2022joj than the rest of the other models, despite showing a redder trend slightly earlier than depicted in the observations. However, this can be attributed to the uncertain explosion time of SN 2022joj.

4.2. Spectra Model Analysis

Figure 8 illustrates the spectral profiles of SN 2022joj both before and after reaching maximum brightness, juxtaposed with thin and thick He-shell double detonation models mentioned in the literature. Shen's $0.979 + 0.02$ and $0.96 + 0.04$ models and Polins's $1.0 + 0.05$ model exhibit striking similarities in spectra with SN 2022joj, including Ti II absorption, a shallow Si II feature, and a lack of O I absorption features ranging from 6 days before maximum light to maximum light. However, discrepancies after maximum light can be attributed to the models assuming LTE, resulting in lower temperatures and more singly ionized Fe group material (Shen et al. 2021a). According to Shen et al. (2021b), the Ti II absorption is due to the lower temperatures caused by both the more radially extended distribution of Ti and the lower flux along these lines of sight. Moreover, Shen $0.979 + 0.02$ more effectively reproduces the early spectrum at -11 days before maximum light and at maximum light. We also measured the Si II velocities of SN 2022joj at maximum light and compared them to the helium double detonation models, most of which overpredicted the velocity of SN 2022joj. SN 2022joj exhibits velocities within the typical range for Type Ia SNe, around 10,000 km s^{-1}. In comparison, the Polin $1.0 + 0.05$ model had a slightly higher velocity at 10,800 km s^{-1}, the Shen $0.96 + 0.04$ model demonstrated a velocity of 12,400 km s^{-1},

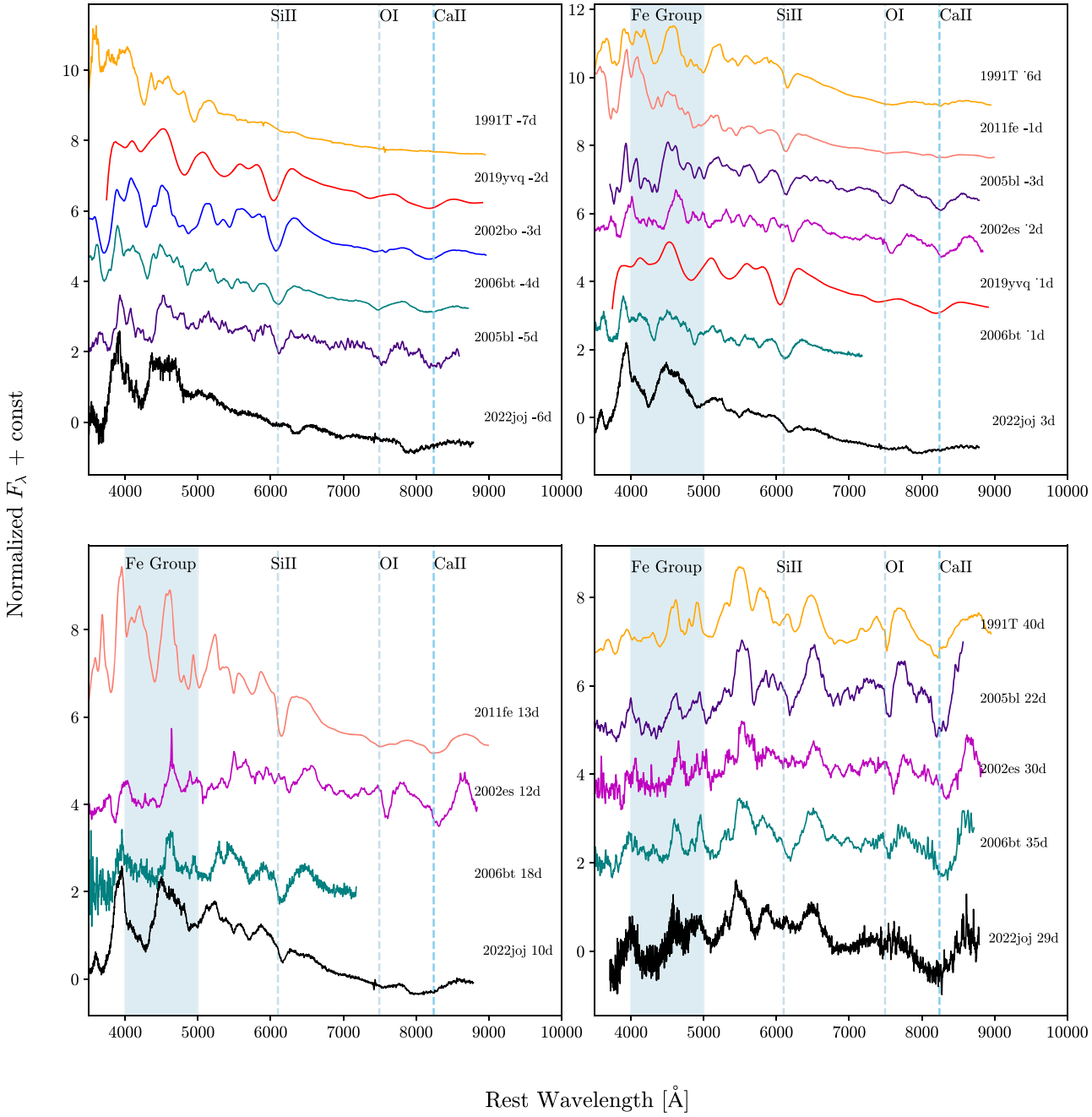

Figure 7. Spectral evolution of SN 2022joj compared with other SNe Ia. The light blue dashed lines show the absorption features created by the respective line labeled at the top of the figure. Note how SN 2022joj resembles subluminous SN spectra (SN 2005bl, whereas the normal SN Ia is SN 2011fe) despite being brighter. The top left panel shows SN 2022joj at early phases. The top right panel shows the spectra of SN 2022joj and other SNe Ia near maximum light. The bottom panels show SN 2022joj after maximum light. Note how SN 2022joj has weak Si II and O I features throughout its evolution and develops a strong Ca II triplet.

the Shen $0.98 + 0.02$ model exhibited a higher velocity of 13,500 km s^{-1}, and the Ni $1.0 + 0.011$ model displayed a velocity of 11,700 km s^{-1}.

Nevertheless, despite Shen's models considering He mixing in the shell with C, the C II 6580 feature at -6 days before maximum light is not reproduced by their models. One possibility for this discrepancy could be that SN 2022joj may contain a significantly higher amount of C in the shell compared to what the models have predicted. An alternative explanation for the absence of this feature could be attributed to the models having computed the spectra under LTE conditions. As highlighted in (Thomas et al. 2007), C II is notably affected by nonthermal processes. By replicating the primary characteristics that distinguish SN 2022joj from typical SN Ia, this model is successful in demonstrating its uniqueness. The differences in the observables of Shen et al. (2021b) to the other models can be attributed to the fact that it was a 2D simulator, which can account for various viewing angles. We found that the best viewing angle (μ, defined as $\cos(\theta)$) that matches SN 2022joj is at $\mu = -0.93$ for the $0.9 + 0.1$ model, $\mu = +0.93$ for the $0.979 + 0.02$, and $\mu = +0$ for the $0.96 + 0.04$. Notably, $\mu = -0.93$ is observed in the southern hemisphere where the carbon-core detonation is ignited, while $\mu = +0.93$ is observed from the northern hemisphere, where

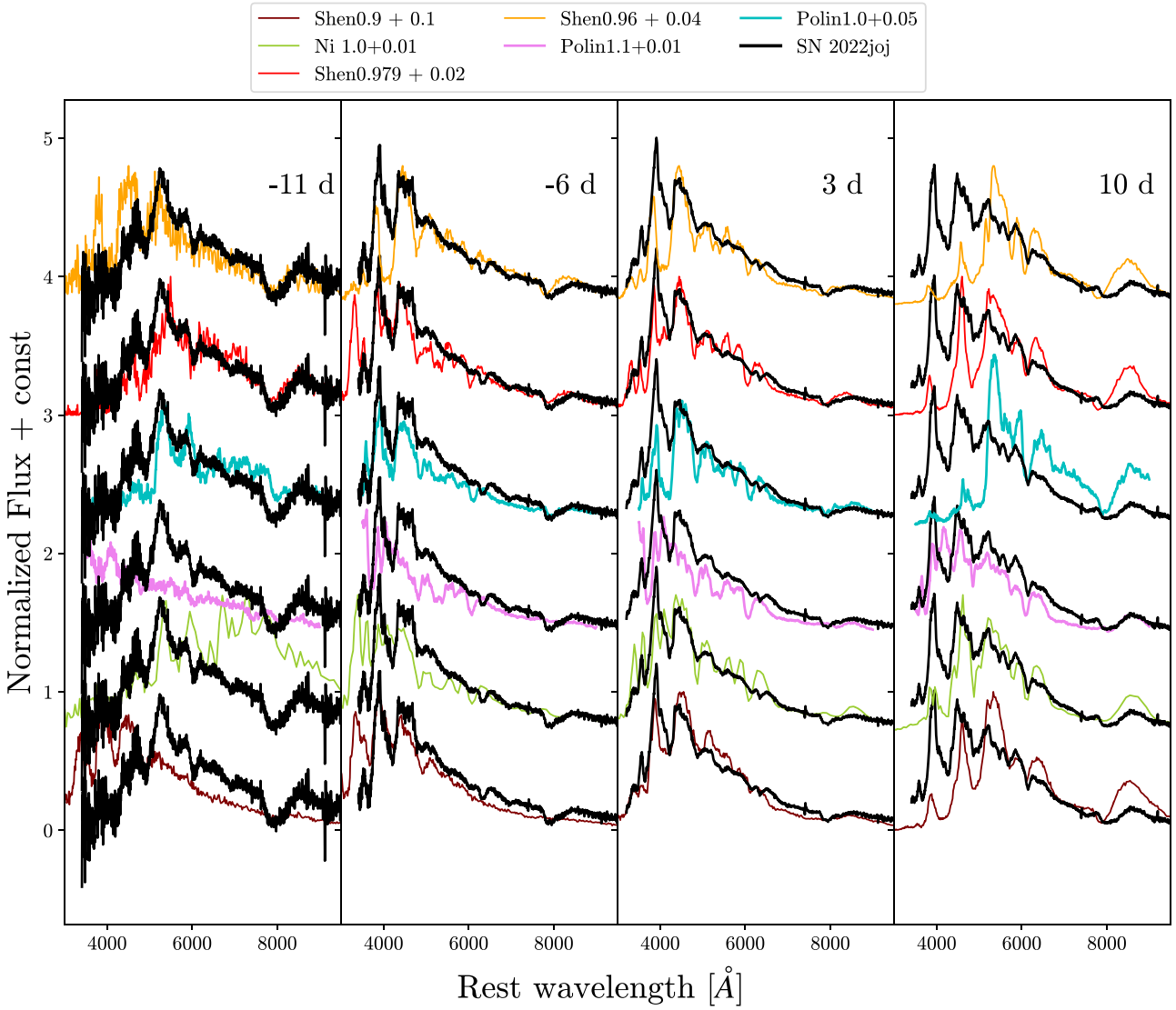

Figure 8. Spectroscopic comparison between SN 2022joj and double detonation models. The left panel shows the spectra at 11 days before maximum light. SN 2022joj shows an extreme reddening and is best matched with Shen 0.979 + 0.02. The second and third panels correspond to 6 days before maximum light and near maximum light. These two panels are best matched with Shen 0.979 + 0.02, Shen 0.9 + 0.1, and Polin 1.2 + 0.01. Lastly, the right panel is 10 days after maximum light, which seems to be best matched with Polin 1.2 + 0.01.

the He is ignited. It is important to note that these chosen matches have drastically different shell thicknesses (at opposite lines of sight), which demonstrates the importance of the multidimensional aspect of the double detonation model. Overall, we find that Shen 0.979 + 0.02 model best matches SN 2022joj spectral peculiarities.

4.3. Nickel Distribution Analysis

Due to the peculiar colors and brightness illustrated in the light curves, we investigate the effects on various nickel distributions. Magee et al. (2018), found that for a given density, models with ^{56}Ni extending through the ejecta were brighter and bluer at earlier times than models in which ^{56}Ni was concentrated. Their models were calculated using TURTLS, a radiative transfer code where the density profile is altered. For each density profile, a series of ^{56}Ni distributions was used, which decrease toward larger radii as shown in Equation (1). The scale parameter s controls how quickly the ejecta transitions from ^{56}Ni-rich to ^{56}Ni-poor, where a larger s represents a sharper transition between the two regions. These scaling parameters ranged from 3–100 and the ^{56}Ni masses from 0.4–0.8 $M_{\odot}$, covering the expected range for typical SNe Ia (Magee et al. 2020).

$$^{56}\mathrm{Ni}(m) = \frac{1}{\exp\left(s[m - M_{\mathrm{Ni}}]/M_{\odot}\right) + 1}. \quad (1)$$

In Figure 10, we plotted the best-fit models for each scaling parameter with the minimum χ^2. From the figure, we notice that the lower the scaling parameter the broader and brighter the early light curve is, due to the ^{56}Ni being farther out than those with a larger scaling parameter (where most of the ^{56}Ni is close to the core). SN 2022joj has a best fit when the scaling parameter is 9.7. Although the light curves are a decent fit, the B band is highly overestimated, indicating that shallower ^{56}Ni distributions predict bluer colors at the early phases, which is the opposite for SN 2022joj. Therefore, a shallower ^{56}Ni cannot explain the early colors seen in SN 2022joj.

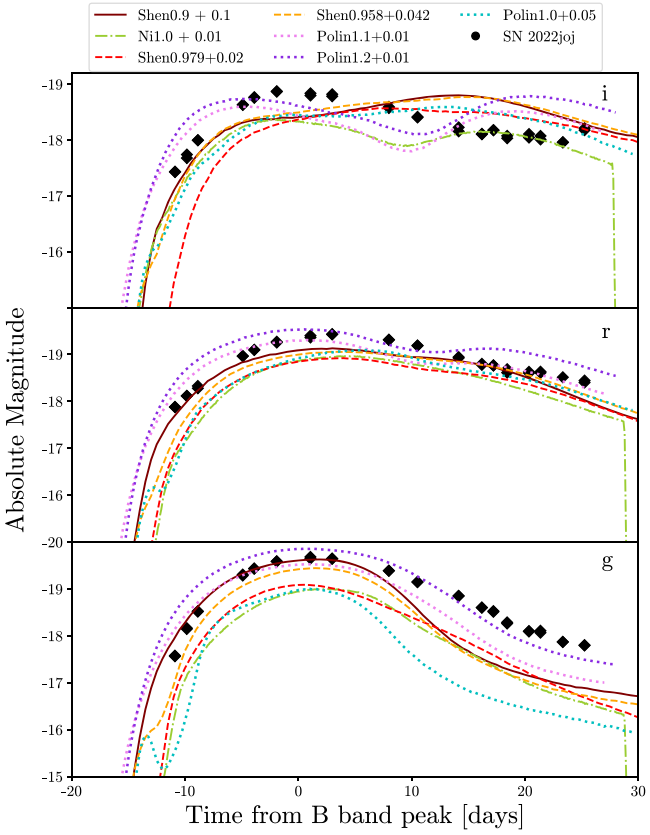

Figure 9. Light-curve comparison between SN 2022joj and double detonation models with a thin and thick He shell. The phase is measured from the *B*-band maximum. It is noteworthy that the majority of models, especially Shen 0.9 + 0.1 and Polin 1.0 + 0.08, effectively capture the light curves of SN 2022joj.

4.4. NIR Analysis

Recent simulations have indicated the presence of unburned helium in both single and double detonations in the outer ejecta (Fink et al. 2010; Shen et al. 2010; Kromer et al. 2010; Sim et al. 2012; Polin et al. 2019; Collins et al. 2022). However, the studies could not fully address the question of whether helium spectral features should form in the models owing to approximations used in the atomic physics in both studies. In Dessart & Hillier (2015), involving non-LTE simulations, it was found that the spectral lines from unburned helium, specifically the He I λ 10830 line, can be observed in the single detonation. The He I λ 10830 line exhibits a P cygni profile and can be visible up to 5 days after explosion. However, the light curves projected by their model are over 2 magnitudes dimmer than SN 2022joj. This is because the models were formulated for single detonation events, which results in fainter observables.

Nonetheless, the He I λ 10830 line has been explored by Boyle et al. (2017) who found that this line could be observed around maximum light and afterward. In Figure 11, we show the NIR spectra of SN 2022joj, along with SN 2016dsg (Dong et al. 2022), SN 2016hnk (Galbany et al. 2019), and the high-mass model of Boyle at 26 days after explosion (+7 days after maximum light). The purpose of this is to illustrate whether there exists unburned He for these double detonation candidates (SN 2022joj, along with SN 2016dsg, SN 2016hnk). In SN 2016dsg, it is suspected that the He line lies somewhere between 9700 and 10,500 Å (Dong et al. 2022). On the other hand, for SN 2016hnk, the absorption feature between 9700 and 10,500 Å is identified as Fe II. Although SN 2022joj seems to be somewhat featureless, there does seem to be a dip around this range that could possibly correspond to the He I feature. This velocity feature appears to be at a lower velocity compared to the model; however, this observation could be influenced by potential Mg II blending. However, a study by Collins et al. (2023), simulated full nonlocal thermodynamic equilibrium radiative transfer models for a double detonation explosion model. At early epochs (5 days after explosion) they found that the He I 10830 was blended with Mg II 10927. However, this feature separates to form a secondary feature while becoming weaker over time. Therefore, we would expect that this feature found in SN 2022joj would have been separated according to Collins et al. (2023) models.

We also plotted the high-mass models from Boyle et al. (2017) based on a progenitor with a CO core mass of 1.025 $M_{\odot}$, and a helium shell mass of 0.055 $M_{\odot}$. The simulation resulted in 0.03 $M_{\odot}$ of unburned helium remaining after explosion and is plotted in Figure 11. It is not surprising that the He I feature in the simulations from Boyle et al. (2017) is stronger than that in SN 2022joj. This difference can be attributed to their models, which assumed a He shell of 0.05 $M_{\odot}$, while the best simulations for SN 2022joj assumed a He shell of 0.02 $M_{\odot}$.

4.5. Nebular Model Analysis

Nebular spectra are a powerful probe of the internal structure of SNe, including geometric asymmetries in the ejecta. Polin et al. (2021) used the 1D hydrodynamic model `SedoNeb` which calculates the emissivities of each atomic transition by solving for the temperature, ionization state, and NLTE level populations. They used the `Sedona` models from Polin et al. (2019) as their input. The 1D models indicate that the prevailing patterns are primarily influenced by the occurrence and arrangement of ^{56}Ni and ^{40}Ca. In particular, they found that low-mass double detonation models with only a small mass fraction of Ca produce nebular spectra that cool primarily through forbidden [Ca II] emission. The more massive progenitors produce spectra with strong Fe lines (4500–5600 Å). However, even their brightest double detonation model overproduces [Ca II] $\lambda\lambda$ 7291, 7323 emission when compared to SNe Ia.

In Figure 12 we show a comparison between SN 2022joj, SN 2018aoz (a double detonation with a thin He-shell candidate), and the modeled double detonation spectra at 150 days after maximum light. Due to the presence of a shallow [Ca II] feature in SN 2022joj, we performed a comparison with the shallowest [Ca II] from the nebular models presented in Polin et al. (2021). It was revealed that these models predict a significantly stronger [Ca II] feature than what was observed for both SN 2022joj and SN 2018aoz as shown in Figure 12. Notably, previous spectroscopic analyses had shown a decent match with Polin 1.2 + 0.01. Therefore, it was surprising to see the disagreement in the nebular phase. These uncertainties could be attributed to atomic data uncertainties and limitations in the 1D simulations; especially since double detonations observations can be highly viewing angle dependent (Shen et al. 2021b).

5. Discussion

5.1. Implications for SN Origins

SN 2022joj appears to disagree with the Phillips relationship, which shows the correlation between the brightness of the SN and the rate of decline (Phillips 1993). Additionally, SN 2022joj shows peculiarity in its colors and classification spectra. SNe Ia typically show a very blue continuum at these

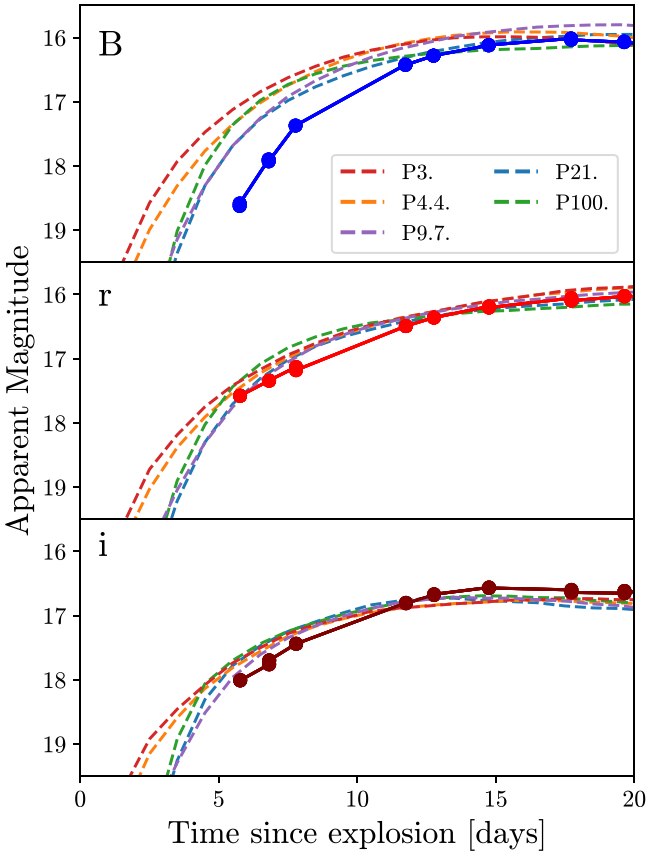

Figure 10. SN 2022joj in the *B*, *r*, and *i* bands among various Ni distributions from Magee et al. (2020). The models assume a Ni mass of 0.8 $M_{\odot}$ and a kinetic energy of 1.4×10^{51} erg. The different values of *P* correspond to the scaling parameter, where the larger values indicate sharper transitions from Ni-rich to Ni-poor.

early phases. In SN 2022joj the colors exhibit an exceptional reddening 11 days prior to reaching maximum light, indicating the presence of a layer that absorbs blue light during these initial stages. This is evident as it appears to be bluer at later phases and reheating is not expected.

When a WD undergoes a double detonation with a thin helium shell, the outer He layer burns to intermediate mass and iron group elements, which can produce strong UV line blanketing and cause a suppression in the blue side of the spectrum ($(\lambda < 5000$ Å); Fink et al. 2010; Shen et al. 2010; Kromer et al. 2010; Sim et al. 2012; Polin et al. 2019; Boos et al. 2021; Collins et al. 2022). We compared the light curves, spectra, and colors of these models to SN 2022joj. It is important to note that LTE models after maximum light are much redder than non-LTE due to low temperatures. Therefore, we observe a mismatch in colors and spectra after maximum light, but we include them for completeness (Shen et al. 2021a). The modeled spectra (especially at maximum light) agree nicely with our data. We found the Shen $0.979 + 0.02$ model to predict reddening at early phases despite having a thin helium shell, it was also the best match spectroscopically to SN 2022joj. More generally, the thinner helium shell models with WD masses around 1 $M_{\odot}$ do a better job at matching the spectral evolution and replicating the suppression of the blue at early phases. Thicker shell models on the other hand tend to show bluer colors at early phases and become a lot redder at later phases. Thinner helium shell masses with WD masses above 1 $M_{\odot}$ also show bluer colors at early phases and generally look more similar to SNe Ia.

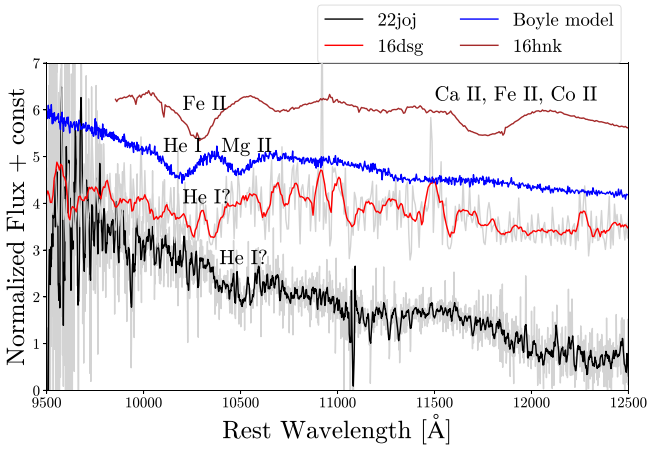

Figure 11. NIR spectra of SN 2022joj plotted against other double detonation candidates and an NIR model from Boyle et al. (2017). Note that the model assumes a He-shell mass of 0.05 $M_{\odot}$ and that the He I absorption feature is more apparent than in the observations. Moreover, SN 2022joj and SN 2016dsg are both plotted at +16 days after reaching maximum brightness, while Boyle's model and SN 2016hnk are depicted at +7 days following their respective peaks.

The light-curve models do a decent job predicting the luminosity of SN 2022joj in particular, although the best spectra model match Shen $0.979 + 0.02$ underpredicts it. Most of the thin helium shells underpredict the luminosity, whereas the thicker helium shell Shen $0.9 + 0.1$ does a better job at matching the brightness but not the shape. Therefore, it is interesting to see that the best light-curve model comes from a thick helium shell rather than a thin one like the spectra models. From Figure 6, we see that the color evolution of double detonation models, in particular the models by Ni $1.0 + 0.01$ and Shen $0.971 + 0.02$, predict extreme reddening at early epochs, consistent with SN 2022joj. The reddening does seem to happen a few days earlier than in SN 2022joj, but this can also be attributed to uncertainties in the explosion time of SN 2022joj. Overall, the double detonation models do a good job at predicting the spectra and colors before and at maximum light. After maximum light, the colors from the models deviate from the data. Again, it is important to note that such deviations are in line with expectations, given the underlying assumption of LTE, and incorporate models for completeness.

Mixing during a subsonic explosion can yield iron group elements in the outer shell of the WD that could explain the reddening observed at the early epochs. This was predicted by some Chandrasekhar-mass explosion models, where a WD initially deflagrates subsonically before transitioning into a detonation (Reinecke et al. 2002). Simulations have shown that when deflagrations occur off-center and are asymmetric, they can generate clusters of Fe peak elements on the surface, which become visible only from certain favorable viewing perspectives (Maeda et al. 2010; Seitenzahl et al. 2013). We compared various ^{56}Ni distributions to SN 2022joj, but found that shallower ^{56}Ni predict bluer colors and broader early light curves.

5.2. Remote Location

At first glance, SN 2022joj appears to be hostless with no nearby galaxy. However, we were able to retrieve deep images[20] secured by the Canada–France–Hawaii Telescope (CFHT), using MegaPrime and their broad single *gri* filter. The

[20] The images were obtained from the Canadian Astronomy Data Center (https://www.cadc-ccda.hia-iha.nrc-cnrc.gc.ca/en/).

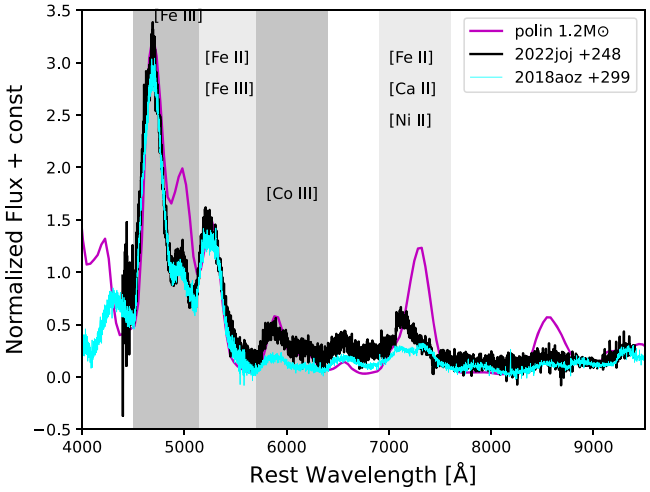

Figure 12. Nebular spectrum of SN 2022joj, double detonation candidate SN 2018aoz, and the model spectra of Polin 1.1 + 0.01 $M_{\odot}$. The model of the nebular spectrum predicts stronger [Ca II] emission than observed for SN 2022joj.

field was observed six times over two epochs (2017 May 19 and April 17), and we stacked them in order to achieve a deeper image. The result is shown in Figure 1, where a spatially resolved host galaxy is clearly detected.

The host appears to be detected in the Pan-STARRS Legacy Survey, which reports a Kron magnitude of 20.8 mag in the *i* band. This apparent magnitude corresponds to an absolute magnitude of −14.3 mag, based on our estimated distance of SN 2022joj (105.2 Mpc), indicating a small dwarf galaxy (Sabatini et al. 2003).

Interestingly, a few double detonation candidates have been found far from their host galaxies—this is considerable given that there is only a handful of double detonation candidates in literature. Notable examples include OGLE-2013-SN-079 (Inserra et al. 2015), SN 2018byg (De et al. 2019), and SN 2016dsg (Dong et al. 2022). SNe with significant displacements have also been detected in numerous Ca-strong transients. One explanation for these Ca-rich transients (theorized to be single detonations of WDs) is that they originate from high-velocity, kicked systems, and explode at considerable distances from their original location within the host galaxy prior to their occurrences (Lyman et al. 2014).

Some alternative progenitor systems with a double detonation include a hot subdwarf B binary with a WD companion (Geier et al. 2013; Kupfer et al. 2022), a WD in a dynamically unstable system where the secondary is either a He WD or a hybrid between He/CO (Guillochon et al. 2010; Pakmor et al. 2013), and a potential outcome is a dynamically driven double degenerate double detonation (D^6) where the companion WD survives the explosion and is flung away (Shen et al. 2018b), and a WD accreting mass from a He star (Neunteufel et al. 2016; Polin et al. 2019).

6. Conclusions

We presented photometric and spectroscopic data of SN 2022joj, a peculiar SN Ia. We tested models with shallow nickel distributions and found that they tend to match the brightness of the SN, but show longer early rise times and brighter early *B*-band flux, contrary to SN 2022joj's behavior. The double detonation models, in particular models with a thin He shell and WD mass at around 1 $M_{\odot}$, were able to explain the light-curve properties of SN 2022joj. Notably, the thin He-shell model offers a more accurate explanation for the spectroscopic features and color evolution observed, in contrast to the thick He-shell model. The double detonation scenario is an attractive explosion mechanism, as it is able to explain the peculiarities of these early observations, especially the early reddening as shown in Figure 6.

Nebular and near-infrared spectra also reveal clues for the progenitor of SN 2022joj. However, neither of the spectra discloses whether SN 2022joj truly is a double detonation. In the NIR spectra, it is unclear if there is any unburned He left from the explosion or whether there may be a possible blend between He I and Mg II. The nebular spectra, on the other hand, pose more of a mystery. Based on the Polin et al. (2021) nebular spectra models of double detonations with a thin He shell, it is expected that the [Ca II] emission feature should be much stronger than observed in SN 2022joj. Moreover, SN 2018aoz does not show a strong [Ca II] either despite being a double detonation candidate. Further modeling is required to test if the double detonation models can explain these objects at all phases, especially nebular observations.

SNe suspected to come from thick-shell helium detonations, like SN 2019eix (Padilla Gonzalez et al. 2023), are different from normal SNe Ia until well after maximum light. However, SN 2022joj, likely from a thin He shell detonation, shows the greatest deviations from normal SNe Ia (red colors and spectra) prior to 10 days before maximum light. After that, it is relatively normal, and is also only one sigma off of the Phillips relation. Not every SN Ia has been observed this early, so such behavior could have easily been missed in large cosmological samples. Furthermore, it raises the question as to whether even thinner He shell detonations are possible. In this case, the evidence could disappear within a day or two, or perhaps within hours of the explosion. SN 2018aoz (Ni et al. 2022) is one such case, which had a brief red color within hours of the explosion, but returned to relative normalcy soon after.

It could be that thin He-shell detonations are the triggering mechanism for the majority of SNe Ia. If this is true it is even more critical to obtain early data for SNe Ia. Until such data are more commonplace, SNe like SN 2022joj provide invaluable insight into the explosion process for at least some SNe. Future studies are necessary to determine if this is an exotic triggering mechanism of 1% of SNe, or if these SNe are just the most obvious examples of a triggering mechanism common to most or even all SNe Ia.

Acknowledgments

We are grateful to the National Science Foundation (NSF) and the University of California, Santa Barbara (UCSB) for funding this project through NSF grants AST-1911225, AST-1911151, and the Central Campus Fellowship.

This research makes use of observations from the Las Cumbres Observatory network, in addition to the MARS ZTF alert broker developed by Las Cumbres Observatory software engineers.

This research has made use of the NASA/IPAC Extragalactic Database (NED) which is operated by the Jet Propulsion Laboratory, California Institute of Technology, under contract with NASA.

This research used the facilities of the Canadian Astronomy Data Center operated by the National Research Council of Canada with the support of the Canadian Space Agency.

Time domain research by D.J.S, and the University of Arizona team is supported by NSF grants AST-1821987,

1813466, 1908972, and 2108032, and by the Heising-Simons Foundation under grant #2020–1864.

Financial support for K.J.S. was in part provided by NASA/ESA Hubble Space Telescope program #15871

Research by Y.D., S.V., and N.M.R is supported by NSF grant AST-2008108.

S.J.B. and D.M.T. acknowledge support from NASA grant HST-AR-16156.

This publication was made possible through the support of an LSSTC Catalyst Fellowship to K.A.B., funded through grant 62192 from the John Templeton Foundation to LSST Corporation. The opinions expressed in this publication are those of the authors and do not necessarily reflect the views of LSSTC or the John Templeton Foundation.

Facilities: HST(STIS), Swift(XRT and UVOT), AAVSO, CTIO:1.3m, CTIO:1.5m, CXO.

Software: `astropy` (Astropy Collaboration et al. 2013, 2018, 2022), `Cloudy` (Ferland et al. 2013), `Source Extractor` (Bertin & Arnouts 1996), `YSE-PZ` (Coulter et al. 2022, 2023).

Appendix

In Tables A1 and Table A2 we present photometric data of SN 2022joj in the BVgri filters using LCO and U,UVW1,

Table A1
Phase with Respect to the B Max where the Dates Are Rounded Up

JD	Epoch	*B*	*V*	*g*	*r*	*i*
2459711	−11	18.62 (0.05)	17.52 (0.04)	17.92 (0.03)	17.58 (0.03)	18.0 (0.03)
2459712	−10	17.90 (0.03)	17.16 (0.02)	17.35 (0.01)	17.34 (0.02)	17.76 (0.04)
2459713	−9	17.37 (0.04)	16.94 (0.04)	16.97 (0.03)	17.13 (0.03)	17.44 (0.05)
2459717	−5	16.42 (0.01)	16.35 (0.01)	16.19 (0.01)	16.49 (0.01)	16.8 (0.01)
2459718	−4	16.28 (0.01)	16.23 (0.02)	16.06 (0.01)	16.36 (0.01)	16.68 (0.01)
2459720	−2	16.12 (0.01)	16.08 (0.02)	15.91 (0.01)	16.19 (0.01)	16.56 (0.01)
2459723	1	16.02 (0.02)	15.96 (0.02)	15.81 (0.01)	16.06 (0.01)	16.6 (0.02)
2459725	3	16.07 (0.02)	15.95 (0.02)	15.85 (0.01)	16.03 (0.01)	16.65 (0.02)
2459730	8	16.47 (0.02)	16.1 (0.02)	16.11 (0.01)	16.15 (0.01)	16.86 (0.03)
2459733	11	16.72 (0.02)	16.21 (0.02)	16.35 (0.01)	16.27 (0.01)	17.02 (0.02)
2459735	12	16.95 (0.03)	…	…	…	…
2459736	14	17.11 (0.02)	16.46 (0.02)	16.64 (0.01)	16.53 (0.01)	17.28 (0.02)
2459738	16	17.44 (0.02)	16.65 (0.02)	16.89 (0.01)	16.68 (0.01)	…
2459739	16	…	…	…	…	17.33 (0.02)
2459740	17	17.46 (0.03)	16.66 (0.02)	16.97 (0.01)	16.69 (0.01)	17.26 (0.03)
2459741	18	17.69 (0.05)	16.81 (0.03)	17.21 (0.02)	16.85 (0.03)	17.36 (0.05)
2459743	20	17.85 (0.04)	16.91 (0.04)	17.4 (0.03)	16.83 (0.02)	17.39 (0.04)
2459744	21	17.85 (0.06)	16.92 (0.04)	17.39 (0.03)	16.85 (0.03)	17.36 (0.06)
2459746	23	18.09 (0.07)	17.06 (0.06)	17.62 (0.04)	16.94 (0.04)	17.48 (0.12)
2459748	25	18.23 (0.03)	17.16 (0.02)	17.7 (0.01)	17.06 (0.07)	17.26 (0.04)
2459753	31	18.63 (0.03)	17.49 (0.02)	18.13 (0.01)	17.23 (0.01)	17.47 (0.02)
2459757	35	18.81 (0.05)	17.71 (0.03)	18.35 (0.03)	17.4 (0.02)	17.57 (0.03)
2459767	44	…	17.98 (0.17)	…	17.88 (0.09)	…
2459772	50	19.41 (0.09)	18.3 (0.05)	18.8 (0.05)	18.23 (0.05)	18.56 (0.07)
2459778	56	19.4 (0.04)	18.48 (0.04)	18.91 (0.03)	18.41 (0.03)	18.78 (0.06)
2459784	62	19.62 (0.07)	18.68 (0.03)	19.04 (0.03)	18.56 (0.03)	18.9 (0.08)
2459787	65	19.63 (0.03)	18.74 (0.04)	19.08 (0.02)	18.63 (0.02)	18.99 (0.11)
2459796	73	19.82 (0.05)	19.07 (0.04)	19.19 (0.03)	18.99 (0.03)	19.35 (0.05)
2459801	78	…	19.17 (0.11)	19.3 (0.08)	19.08 (0.08)	…
2459805	83	19.91 (0.04)	…	…	…	…
2459806	83	…	19.22 (0.04)	19.36 (0.03)	19.22 (0.05)	19.78 (0.1)
2459810	88	19.97 (0.04)	19.31 (0.04)	19.45 (0.02)	19.39 (0.03)	…
2459811	88	…	…	…	19.42(0.04)	19.84 (0.07)

Note. Note that the photometry in this table does not account for extinction; however, the Milky Way extinction value, $E(B-V) = 0.0313$, yields a *U*: 0.1532, *B*: 0.1281, *g*: 0.116, *V*: 0.0962, *r*: 0.080, *i*: 0.05912 correction per filter.

Table A2
Swift+UVOT Photometry

JD	Epoch	*UV-W2*	*UV-M2*	*UV-W1*	*U*	*B*	*V*
2459716.88	−5.42	>20.68	>20.81	19.19(0.29)	17.26(0.09)	16.37(0.04)	16.38(0.06)
2459720.56	−1.74	19.37(0.15)	>20.37	18.14(0.11)	16.55(0.06)	16.05(0.03)	16.03(0.04)
2459720.96	−1.34	19.43(0.15)	19.59(0.22)	18.19(0.11)	16.70(0.06)	16.03(0.03)	15.93(0.04)
2459723.25	0.95	19.35(0.13)	20.22(0.30)	18.52(0.16)	16.57(0.05)	15.99(0.03)	15.94(0.03)

Note. Magnitudes are in the Vega system. Phase is with respect to the B max.

UVW2, and UVM2, using the Neil Gehrels Swift Observatory, respectively.

ORCID iDs

E. Padilla Gonzalez https://orcid.org/0000-0003-0209-9246
D. A. Howell https://orcid.org/0000-0003-4253-656X
G. Terreran https://orcid.org/0000-0003-0794-5982
C. McCully https://orcid.org/0000-0001-5807-7893
M. Newsome https://orcid.org/0000-0001-9570-0584
J. Burke https://orcid.org/0000-0003-0035-6659
J. Farah https://orcid.org/0000-0003-4914-5625
C. Pellegrino https://orcid.org/0000-0002-7472-1279
K. A. Bostroem https://orcid.org/0000-0002-4924-444X
G. Hosseinzadeh https://orcid.org/0000-0002-0832-2974
J. Pearson https://orcid.org/0000-0002-0744-0047
D. J. Sand https://orcid.org/0000-0003-4102-380X
M. Shrestha https://orcid.org/0000-0002-4022-1874
N. Smith https://orcid.org/0000-0001-5510-2424
Y. Dong (董一泽) https://orcid.org/0000-0002-7937-6371
N. Meza Retamal https://orcid.org/0000-0002-7015-3446
S. Valenti https://orcid.org/0000-0001-8818-0795
S. Boos https://orcid.org/0000-0002-1184-0692
K. J. Shen https://orcid.org/0000-0002-9632-6106
D. Townsley https://orcid.org/0000-0002-9538-5948
L. Galbany https://orcid.org/0000-0002-1296-6887
R. J. Foley https://orcid.org/0000-0002-2445-5275
M. J. Bustamante-Rosell https://orcid.org/0000-0003-0416-9818
D. A. Coulter https://orcid.org/0000-0003-4263-2228
R. Chornock https://orcid.org/0000-0002-7706-5668
K. W. Davis https://orcid.org/0000-0002-5680-4660
C. B. Dickinson https://orcid.org/0000-0001-9749-4200
D. O. Jones https://orcid.org/0000-0002-6230-0151
J. Kutcka https://orcid.org/0009-0004-7605-8484
X. K. Le Saux https://orcid.org/0009-0004-3242-282X
C. R. Rojas-Bravo https://orcid.org/0000-0002-7559-315X
K. Taggart https://orcid.org/0000-0002-5748-4558
S. Tinyanont https://orcid.org/0000-0002-1481-4676
G. Yang https://orcid.org/0000-0001-7823-2627
S. W. Jha https://orcid.org/0000-0001-8738-6011
R. Margutti https://orcid.org/0000-0003-4768-7586

References

Albareti, F., Allende Prieto, C., Almeida, A., et al. 2017, ApJS, 233, 25
Almgren, A. S., Beckner, V. E., Bell, J. B., et al. 2010, ApJ, 715, 1221
Astropy Collaboration, Robitaille, T. P., Tollerud, E. J., et al. 2013, A&A, 558, A33
Astropy Collaboration, Price-Whelan, A. M., Sipőcz, B. M., et al. 2018, AJ, 156, 123
Astropy Collaboration, Price-Whelan, A. M., Lim, P. L., et al. 2022, ApJ, 935, 167
Bertin, E., & Arnouts, S. 1996, A&AS, 117, 393
Bessel, M. S. 1990, A&AS, 83, 357
Bildsten, L., Shen, K. J., Weinberg, N. N., & Nelemans, G. 2007, ApJL, 662, L95
Blondin, S., Dessart, L., & Hillier, D. J. 2018, MNRAS, 474, 3931
Blondin, S., & Tonry, J. L. 2007, ApJ, 666, 1024
Boos, S. J., Townsley, D. M., Shen, K. J., Caldwell, S., & Miles, B. J. 2021, ApJ, 919, 126
Boyle, A., Sim, S. A., Hachinger, S., & Kerzendorf, W. 2017, A&A, 599, A46
Brown, T. M., Baliber, N., & Bianco, F. 2013, PASP, 125, 1031
Brown, P. J., Holland, S. T., Immler, S., et al. 2009, AJ, 137, 4517
Catalán, S., Isern, J., García-Berro, E., & Ribas, I. 2008, MNRAS, 387, 1693
Chen, M. C., Herwig, F., Denissenkov, P. A., & Paxton, B. 2014, MNRAS, 440, 1274
Collins, C. E., Gronow, S., Sim, S. A., & Röpke, F. K. 2022, MNRAS, 517, 5289
Collins, C. E., Sim, S. A., Shingles, L. J., et al. 2023, MNRAS, 524, 4447
Coulter, D. A., Jones, D. O., McGill, P., et al. 2022, YSE-PZ: An Open-source Target and Observation Management System, v0.3.0, Zenodo,doi:10.5281/zenodo.7278430
Coulter, D. A., Jones, D. O., McGill, P., et al. 2023, PASP, 135, 064501
Cushing, M. C., Vacca, W. D., & Rayner, J. T. 2004, PASP, 116, 362
De, K., Kasliwal, M. M., Polin, A., et al. 2019, ApJL, 873, L18
Dessart, L., & Hillier, D. J. 2015, MNRAS, 447, 1370
Dominguez, I., Chieffi, A., Limongi, M., & Straniero, O. 1999, ApJ, 524, 226
Dong, Y., Valenti, S., Polin, A., et al. 2022, ApJ, 934, 102
Dubey, A., Antypas, K., Calder, A. C., et al. 2014, Int. J. High Perform. Comput. Appl., 28, 225
Fabricant, D., Fata, R., Epps, H., et al. 2019, PASP, 131, 075004
Ferland, G. J., Porter, R. L., van Hoof, P. A. M., et al. 2013, RMxAA, 49, 137
Filippenko, A., Richmond, M., Branch, D., et al. 1992, AJ, 104, 1543
Fink, M., Röpke, F. K., Hillebrandt, W., et al. 2010, A&A, 514, A53
Flewelling, H. A., Magnier, E. A., Chambers, K. C., et al. 2020, ApJS, 251, 7
Foley, R. J., Narayan, G., Challis, P. J., et al. 2010, ApJ, 708, 1748
Fremling, C. 2022, Transient Name Server Discovery Report 2022-167, TNS
Fukugita, M., Ichikawa, T., Gunn, J. E., et al. 1996, AJ, 111, 1748
Galbany, L., Ashall, C., Höflich, P., et al. 2019, A&A, 630, A76
Ganeshalingam, M., Li, W., Filippenko, A. V., et al. 2012, ApJ, 751, 142
Gehrels, N., Chincarini, G., & Giommi, P. 2004, ApJ, 611, 1005
Geier, S., Marsh, T. R., Wang, B., et al. 2013, A&A, 554, A54
Girardi, L., Bertelli, G., Bressan, A., et al. 2002, A&A, 391, 195
Guillochon, J., Dan, M., Ramirez-Ruiz, E., & Rosswog, S. 2010, ApJL, 709, L64
Henden, A. A., Welch, D. L., Terrell, D., & Levine, S. E. 2009, AAS Meeting 214, 407.02
Iben, I. J., & Tutukov, A. V. 1984, ApJS, 54, 335
Inserra, C., Sim, S. A., Wyrzykowski, L., et al. 2015, ApJL, 799, L2
Iwamoto, K., Brachwitz, F., Nomoto, K., et al. 1999, ApJS, 125, 439
Jiang, J.-A., Doi, M., Maeda, K., et al. 2017, Natur, 550, 80
Kansky, J., Chilingarian, I., Fabricant, D., et al. 2019, PASP, 131, 075005
Kasen, D. 2006, ApJ, 649, 939
Kasen, D., Thomas, R. C., & Nugent, P. 2006, ApJ, 651, 366
Khokhlov, A. M. 1991, A&A, 245, 114
Kromer, M., & Sim, S. A. 2009, MNRAS, 398, 1809
Kromer, M., Sim, S. A., Fink, M., et al. 2010, ApJ, 719, 1067
Kupfer, T., Bauer, E. B., van Roestel, J., et al. 2022, ApJL, 925, L12
Liu, C., Miller, A. A., Boos, S. J., et al. 2023, ApJ, 958, 178
Lyman, J. D., Levan, A. J., Church, R. P., Davies, M. B., & Tanvir, N. R. 2014, MNRAS, 444, 2157
Maeda, K., Röpke, F., Fink, M., et al. 2010, ApJ, 712, 624
Magee, M. R., Maguire, K., Kotak, R., et al. 2020, A&A, 634, A37
Magee, M. R., Sim, S. A., Kotak, R., & Kerzendorf, W. E. 2018, A&A, 614, A115
Mazzali, P., Chugai, N., Turatto, M., et al. 1997, MNRAS, 284, 151
Mazzali, P. A., Deng, J., Maeda, K., et al. 2002, ApJL, 572, L61
Meng, X., & Podsiadlowski, P. 2014, ApJL, 789, L45
Moore, K., Townsley, D. M., & Bildsten, L. 2013, ApJ, 776, 97
Neunteufel, P., Yoon, S. C., & Langer, N. 2016, A&A, 589, A43
Newsome, M., Li, W., Burke, J., et al. 2022, Transient Name Server Classification Report 2022-2167, TNS
Ni, Y. Q., Moon, D.-S., Drout, M. R., et al. 2022, NatAs, 6, 568
O'Brien, J. T., Kerzendorf, W. E., Fullard, A., et al. 2021, ApJL, 916, L14
Padilla Gonzalez, E., Howell, D. A., Burke, J., et al. 2023, ApJ, 953, 25
Pakmor, R., Kromer, M., Taubenberger, S., & Springel, V. 2013, ApJL, 770, L8
Perets, H., Gal-Yam, A., & Mazzali, P. 2010, Natur, 465, 322
Perlmutter, S., Aldering, G., Goldhaber, G., et al. 1999, ApJ, 517, 565
Phillips, M. M. 1993, ApJL, 413, L105
Polin, A., Nugent, P., & Kasen, D. 2019, ApJ, 873, 84
Polin, A., Nugent, P., & Kasen, D. 2021, ApJ, 906, 65
Prochaska, J. X., Hennawi, J. F., Westfall, K. B., et al. 2020, JOSS, 5, 2308
Reinecke, M., Hillebrandt, W., & Niemeyer, J. C. 2002, A&A, 391, 1167
Riess, A. G., Filippenko, A. V., Challis, P., et al. 1998, AJ, 116, 1009
Roming, P., Kennedy, W., & Mason, K. M. 2005, SSRv, 120, 95
Ruiter, A. J., Sim, S. A., Pakmor, R., et al. 2013, MNRAS, 429, 1425
Sabatini, S., Roberts, S., & Davies, J. 2003, in Galaxy Evolution in Groups and Clusters, ed. C. Lobo, M. Serote Roos, & A. Biviano (Dordrecht: Kluwer), 97
Sánchez-Sáez, P., Reyes, I., Valenzuela, C., et al. 2021, AJ, 161, 141
Schlafly, E. F., & Finkbeiner, D. P. 2011, ApJ, 737, 103

Schlegel, D. J., Finkbeiner, D. P., & Davis, M. 1998, ApJ, 500, 525
Seitenzahl, I. R., Ciaraldi-Schoolmann, F., Röpke, F. K., et al. 2013, MNRAS, 429, 1156
Shen, K. J., & Bildsten, L. 2014, ApJ, 785, 61
Shen, K. J., Blondin, S., Kasen, D., et al. 2021a, ApJL, 909, L18
Shen, K. J., Boos, S. J., Townsley, D. M., & Kasen, D. 2021b, ApJ, 922, 68
Shen, K. J., Boubert, D., Gänsicke, B. T., et al. 2018b, ApJ, 865, 15
Shen, K. J., Kasen, D., Miles, B. J., & Townsley, D. M. 2018a, ApJ, 854, 52
Shen, K. J., Kasen, D., & Weinberg, N. N. 2010, ApJS, 715, 767
Sim, S. A., Fink, M., & Kromer, M. 2012, MNRAS, 420, 3003
Sim, S. A., Röpke, F. K., Hillebrandt, W., et al. 2010, ApJL, 714, L52
Taubenberger, S., Hachinger, S., Pignata, G., et al. 2008, MNRAS, 385, 75
Thomas, R. C., Aldering, G., Antilogus, P., et al. 2007, ApJL, 654, L53
Townsley, D. M., Miles, B. J., Shen, K. J., & Kasen, D. 2019, ApJL, 878, L38
Valenti, S., Howell, D. A., Stritzinger, M. L., et al. 2016, MNRAS, 459, 3939
Valenti, S., Yuan, F., & Taubenberger, S. 2014, MNRAS, 437, 1519
Webbink, R. F. 1984, ApJ, 277, 355
Whelan, R. F., & Iben, I. J. 1973, ApJ, 186, 1007
Wilson, J. C., Henderson, C. P., Herter, T. L., et al. 2004, Proc. SPIE, 5492, 1295
Wolf, W. M., Bildsten, L., Brooks, J., & Paxton, B. 2013, ApJ, 777, 136
Woosley, S. E., & Weaver, T. A. 1994, ApJ, 423, 371